Journal of Applied Physics ARTICLE pubs.aip.org/aip/jap

Writing and reading magnetization states via strain in Fe_3GaTe_2/*h*-BN/$MnBi_2Te_4$ junction

Cite as: J. Appl. Phys. **135**, 174303 (2024); doi: 10.1063/5.0202687
Submitted: 6 February 2024 · Accepted: 3 April 2024 ·
Published Online: 1 May 2024

View Online Export Citation CrossMark

Li Deng,[1] Xiang Yin,[1] Junwei Tong,[2] Yanzhao Wu,[1] Fubo Tian,[3] and Xianmin Zhang[1,a)]

AFFILIATIONS

[1]Key Laboratory for Anisotropy and Texture of Materials (Ministry of Education), School of Material Science and Engineering, Northeastern University, Shenyang 110819, China
[2]Department of Physics, Freie Universität Berlin, Berlin 14195, Germany
[3]State Key Laboratory of Superhard Materials, College of Physics, Jilin University, Changchun 130012, China

[a)]**Author to whom correspondence should be addressed:** zhangxm@atm.neu.edu.cn

ABSTRACT

Writing and reading of magnetization states via mechanical strain are crucial for the development of ultralow-power spintronic devices. In this study, a van der Waals magnetic tunnel junction (vdW MTJ) of Fe_3GaTe_2/*h*-BN/$MnBi_2Te_4$ is constructed to explore the magnetization reversal under in-plane biaxial strains. Interestingly, the interlayer magnetic coupling of devices can be tuned to ferromagnetic and antiferromagnetic states by tensile and compressive strains, respectively. The various magnetic couplings on applied strains are analyzed using the superexchange theory. Importantly, the interlayer coupling nearly vanishes after removing external strains, ensuring the nonvolatility of magnetization reversal, resulting in the nonvolatile writing of magnetization states in the present vdW MTJ. Moreover, the tunneling magnetoresistance ratio of the device is up to −5745%, which remains −1478% even with −2% strain, showing great potential for reading the magnetization states. Therefore, this work provides an alternate avenue to write and read magnetization states in one vdW MTJ under biaxial strains.

I. INTRODUCTION

Two-dimensional (2D) magnetic materials have opened up exciting possibilities for designing van der Waals magnetic tunnel junctions (vdW MTJs).[1–4] Similar to the structure of conventional MTJs,[5–8] the vdW MTJs are vertically stacked with two ferromagnetic (FM) electrodes and a nonmagnetic spacer. Notably, the unique electronic behaviors of 2D FM electrodes present two significant advantages for vdW MTJs over their conventional counterparts. On the one hand, the absence of dangling bonds could result in cleaner interfaces, leading to better transport properties of vdW MTJs.[9,10] On the other hand, the vdW MTJs conform to the curved surfaces, expanding their flexible applications.[11,12] A vital performance of vdW MTJs relates to the fact that the tunneling magnetoresistance (TMR) effect offers an effective means of reading magnetization states.[13–16] The vdW MTJ of graphene (Gr)/CrI_3/Gr showed a giant TMR of up to 19 000% with four-layer CrI_3 as tunnel barriers,[1] which is an order of magnitude larger than that of MgO-based conventional MTJs.[7,8] A field induced metamagnetic transition was observed in the Gr/CrI_3/Gr devices, resulting in a TMR of 95%, 300%, and 550% for bilayer, trilayer, and tetralayer CrI_3 barriers, respectively.[2] In recent years, Fe_3GaTe_2 and Fe_3GeTe_2 have been widely used to construct all-2D MTJs, showing very interesting results for next-generation memory devices.[17–21] Therefore, vdW MTJs have exhibited tremendous potential for the application of spin devices and the exploration of fundamental science.[3,4,9–16,22,23]

Writing magnetization states in vdW MTJs with excellent reproductivity and nonvolatility is the other core issue for magnetic information storage in spintronics,[24–27] which is usually determined by the magnetization reversal from the antiferromagnetic (AFM) to the FM state and vice versa. An interlayer transition from AFM to FM interaction was demonstrated in atomically thin CrI_3 through a hydrostatic pressure, but the transition was irreversible.[28,29] Fortunately, Cenker *et al.* predicted and achieved a reversible strain-manipulated phase transition from an interlayer AFM to an FM state in a vdW CrSBr magnet.[30] Based on first-principles

calculations, Zhu *et al.* predicted a reversible strain-induced switching from AFM to FM coupling in bilayer MnS_2.[31] The nonvolatility of writing operation means the data can be maintained in the device after removing the external stimulus such as an electric field or magnetic field.[32] Cheng *et al.* showed a nonvolatile control of interlayer coupling between the AFM and the FM state in bilayer CrI_3/In_2Se_3 vdW heterostructures by tuning the polarization of 2D ferroelectric In_2Se_3.[33] Through the support of various ferroelectric layers, the nonvolatile writing of magnetization states has been explored.[34,35] Nevertheless, the magnetization reversal speed would be seriously limited by ferroelectric response and instable interface.[36,37] Most recently, the Dzyaloshinskii–Moriya interaction torque was proposed to obtain magnetization switching controlled by voltage pulses, which was demonstrated in 2D multiferroics, $CuCrP_2Se_6$, and CrN, using first-principles calculations and micromagnetic simulations.[38] Although the above progress has been made, the writing and reading of magnetization states in vdW MTJs are still full of challenges for practical applications. The explorations of an efficient approach and intrinsic mechanism are highly desired to achieve a nonvolatile magnetization reversal in vdW MTJs.

Here, we study the writing and reading of magnetization states in vdW MTJs through strain regulation caused by the sensitive response of 2D materials, which is valuable for flexible spintronics with energy efficiency. A vdW MTJ with a Fe_3GaTe_2/h-BN/$MnBi_2Te_4$ stacking structure is constructed to explore the magnetization reversal by applying strains. By investigating the interlayer coupling of the device under different biaxial strains, the device can be tuned to FM and AFM states by tensile and compressive strains, respectively. Importantly, the interlayer coupling nearly vanishes after the external strain is removed, ensuring the nonvolatility of the magnetization reversal. As a result, the nonvolatile writing of magnetization states by strain is successfully realized in the vdW MTJ. Furthermore, the TMR ratio reaches an impressive value of −5745% without strain and remains −1478% even with −2% strain, showing great potential for reading the magnetization states. Therefore, the present study provides an alternate method to write and read magnetization states for flexible spintronic devices with the advantage of both ultralow-power consumption and high-density storage.

II. METHODS

First-principles calculations are performed using the density functional theory (DFT) within the Vienna *ab initio* Simulation Package (VASP).[39,40] The Perdew, Burke, and Ernzerhof (PBE) generalized gradient approximation (GGA) functional is employed.[41] The projector augmented wave (PAW) method[42] is used with a cutoff energy of 500 eV. To account for the 3d orbitals of the Mn atom, an effective Hubbard U (U_{eff}) value of 4 eV is considered based on Dudarev's approach[43] The first Brillouin zone is sampled using a Γ-centered $15 \times 15 \times 1$ Monkhorst-Pack grid.[44] A vacuum space of 20 Å is utilized to model the 2D system. The convergence criteria for energy and Hellmann–Feynman force components are set to 1×10^{-9} eV and 0.001 eV/Å, respectively. The vdW correction is incorporated using the Grimme's DFT-D3 scheme.[45,46] The magnetic anisotropy calculations include the spin–orbit coupling (SOC) effect. The VASP data are processed using the VASPKIT code.[47]

For the investigation of spin-dependent transport properties for the Gr/Fe_3GaTe_2/h-BN/$MnBi_2Te_4$/Gr device, the self-consistent Non-Equilibrium Green's Function (NEGF) formalism technique is employed using the TranSIESTA code.[48–50] The Troullier–Martins (TM) norm-conserving pseudopotentials (NCPP) are utilized.[51] The single-ζ basis is employed for Gr, while the double-ζ plus polarization basis is used for Fe_3GaTe_2, *h*-BN, and $MnBi_2Te_4$. A cutoff energy of 300 Ry and a mixing rate of 0.02 are chosen for the self-consistent calculations. The density matrix and transmission coefficients are calculated using 15×15 and 101×101 *k* meshes, respectively. The convergence criterion for the density matrix is set to 5×10^{-5} eV. More details can be found in the supplementary material.

III. RESULTS AND DISCUSSIONS

A. Strain regulates electronic and magnetic properties

Fe_3GaTe_2 is a 2D vdW intrinsic ferromagnet with strong perpendicular magnetic anisotropy (PMA) and a high Curie temperature of over 300 K, making it a promising candidate for room-temperature spintronic devices.[52,53] As shown in Fig. 1(a), the Fe_3GaTe_2 monolayer has a hexagonal structure belonging to the $P\bar{6}m2$ space group, with the Fe_3Ga heterometallic slab sandwiched between two Te layers.[52] In Fig. 1(b), the spin-resolved energy band and density of states (DOS) for Fe_3GaTe_2 demonstrate its FM metallic behavior. Considering the spin–orbit coupling (SOC) interaction, the magnetic anisotropy energy (MAE) is calculated as $MAE = E_\theta - E_z$, where E_θ and E_z represent the total energy of the system with magnetic moments along the θ and [001] directions, respectively. The variation of the MAE with θ plotted in Fig. 1(c) confirms that the Fe_3GaTe_2 monolayer exhibits PMA. On the other hand, $MnBi_2Te_4$ is chosen as the other magnetic layer in the vdW MTJ with tunable magnetism and topological features, showing potential application in novel spintronic devices.[54,55] Figure 1(d) shows the crystal structure of a $MnBi_2Te_4$ monolayer that belongs to the space group of $P\bar{3}m1$. It consists of seven atomic layers arranged as Te–Bi–Te–Mn–Te–Bi–Te, where Mn atoms in the central plane form a triangular lattice.[55] The energy band and DOS in Fig. 1(e) reveal that $MnBi_2Te_4$ is an FM semiconductor, exhibiting a half-semiconductor characteristic with a potentially high spin-polarization. The spin-resolved bandgaps of the spin- up and spin-down channels are 1.00 and 1.27 eV, respectively, which are in agreement with those of previous studies.[56] Figure 1(f) indicates that the easy axis of the $MnBi_2Te_4$ monolayer is also perpendicular to the *xy* plane.

The effects of strain on the magnetic anisotropy and intralayer magnetic coupling of the Fe_3GaTe_2 and $MnBi_2Te_4$ monolayers are investigated prior to constructing the vdW MTJ. The in-plane biaxial (ϵ) strain ranging from −2% to 4% is applied to examine the magnetic properties of the Fe_3GaTe_2 and $MnBi_2Te_4$ monolayers, where ϵ is defined as $\epsilon = (a - a_0)/a_0$. The a and a_0 are the lattice constants with and without strain, respectively. Figure 2(a) shows the MAE of Fe_3GaTe_2 as a function of biaxial strain. It is observed that the MAE initially decreases and then increases dramatically, reaching around 1837 μeV per unit cell with a tensile strain of over 2%, while for the compressive strain, there is only a slight increase in the MAE of Fe_3GaTe_2. The variation of the MAE

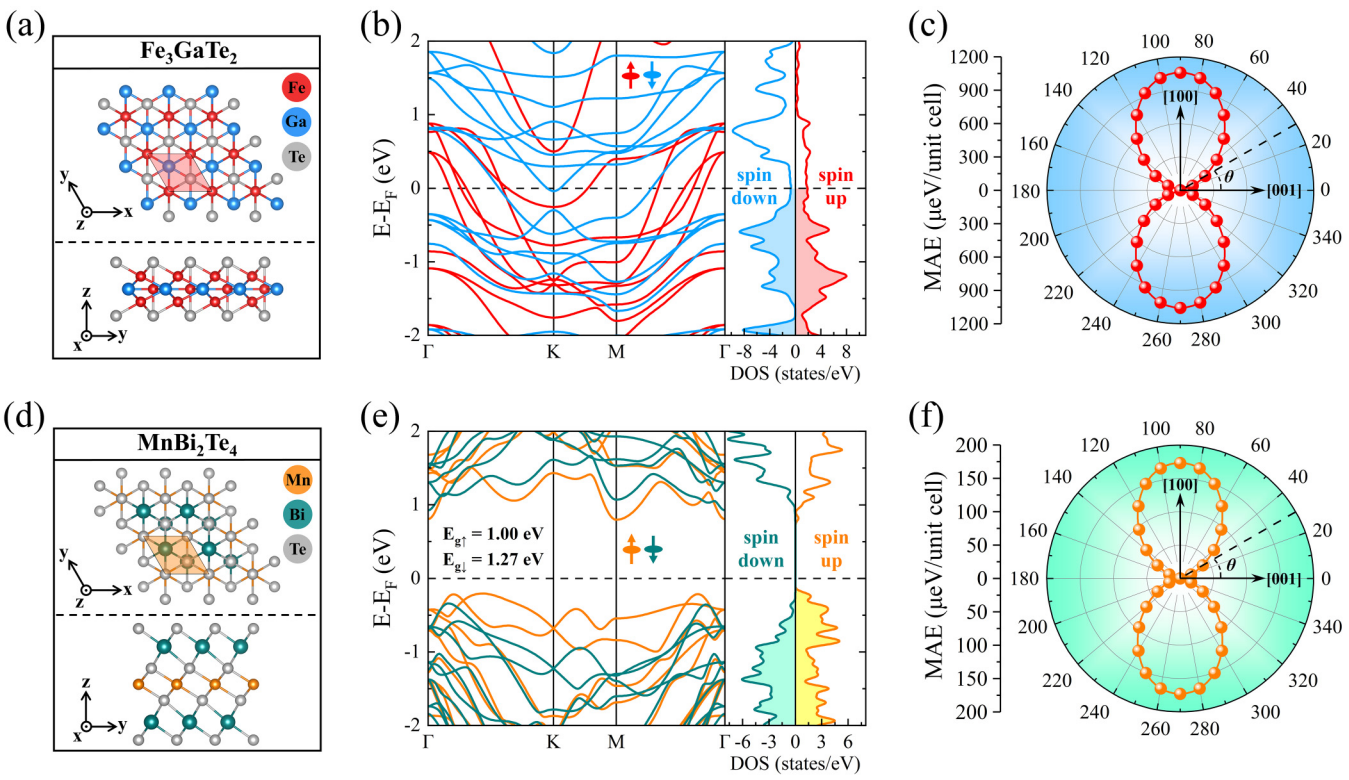

FIG. 1. Structures, energy bands, DOSs, and MAEs for monolayers. (a) Schematic illustration of the crystal structure for the Fe_3GaTe_2 monolayer. (b) Spin-resolved energy band and DOS of Fe_3GaTe_2. The red (blue) line represents the spin-up (down) band. (c) MAE of Fe_3GaTe_2 as a function of θ in polar coordinates. (d) Schematic illustration of the crystal structure for the $MnBi_2Te_4$ monolayer. (e) Spin-resolved energy band and DOS of $MnBi_2Te_4$. The orange (cyan) line represents the spin-up (down) band. $E_{g\uparrow}$ ($E_{g\downarrow}$) represents the bandgap of the spin-up (spin-down) channel. (f) MAE of $MnBi_2Te_4$ as a function of θ in polar coordinates.

for $MnBi_2Te_4$ with applied strain is plotted in Fig. 2(b), which shows a monotonically decreasing trend of the MAE with the increase in strain. Despite the effects of strain on the magnitude of MAEs for Fe_3GaTe_2 and $MnBi_2Te_4$, the sign of the MAE remains positive. This indicates that both the Fe_3GaTe_2 and $MnBi_2Te_4$ monolayers maintain their PMA behavior within the range of applied strain. To investigate the intralayer magnetic coupling of Fe_3GaTe_2 and $MnBi_2Te_4$ under the strain, four magnetic configurations of FM, AFM1, AFM2, and AFM3 (see Fig. S1 in the supplementary material) are considered. The exchange energy (ΔE_{ex}) is calculated as $\Delta E_{ex} = E_{intra\_AFM} - E_{intra\_FM}$, where E_{intra_AFM} and E_{intra_FM} are the energies of the system with intralayer AFM and FM coupling, respectively. As illustrated in Fig. 2(c), both the tensile and the compressive strains lead to a decrease in the ΔE_{ex} of Fe_3GaTe_2. Comparatively, for $MnBi_2Te_4$ shown in Fig. 2(d), ΔE_{ex} decreases and increases with the tensile and compressive strains, respectively. Notably, the values of ΔE_{ex} for Fe_3GaTe_2 and $MnBi_2Te_4$ shown in Figs. 2(c) and 2(d) are always positive, demonstrating the stability of intralayer FM coupling under the applied strain. Overall, these results indicate that Fe_3GaTe_2 and $MnBi_2Te_4$ monolayers exhibit a stable PMA and intralayer FM coupling under strain, making them suitable for constructing the vertical vdW MTJ to explore magnetization reversal controlled by strain.

B. Writing magnetization states by strain

To investigate the feasibility of manipulating magnetization reversal by strain, a vdW MTJ of Fe_3GaTe_2/*h*-BN/$MnBi_2Te_4$ is constructed by vertically stacking the Fe_3GaTe_2 monolayer, hexagonal boron nitride (*h*-BN) monolayer, and $MnBi_2Te_4$ monolayer, after optimizing the stacking types (see Fig. S2 in the supplementary material). The device structure is illustrated in Fig. 3(a), where the 2D insulating *h*-BN layer serves as a spacer to reduce the interlayer coupling between Fe_3GaTe_2 and $MnBi_2Te_4$. The fixed layer is the $MnBi_2Te_4$ monolayer because of its small MAE compared with that of Fe_3GaTe_2, as shown in Fig. 2. The magnetic moments of the Mn atom in $MnBi_2Te_4$ are along the positive direction of the *z* axis. The magnetization direction of the free layer Fe_3GaTe_2 can be switched between parallel and antiparallel to that of $MnBi_2Te_4$, resulting in two distinct magnetization states, FM and AFM states, as shown at the bottom of Fig. 3(a). The goal is to achieve the switching between FM and AFM states by applying an in-plane biaxial strain to the device. Figures 3(b) and S3 in the supplementary material depict the spin- and atom-

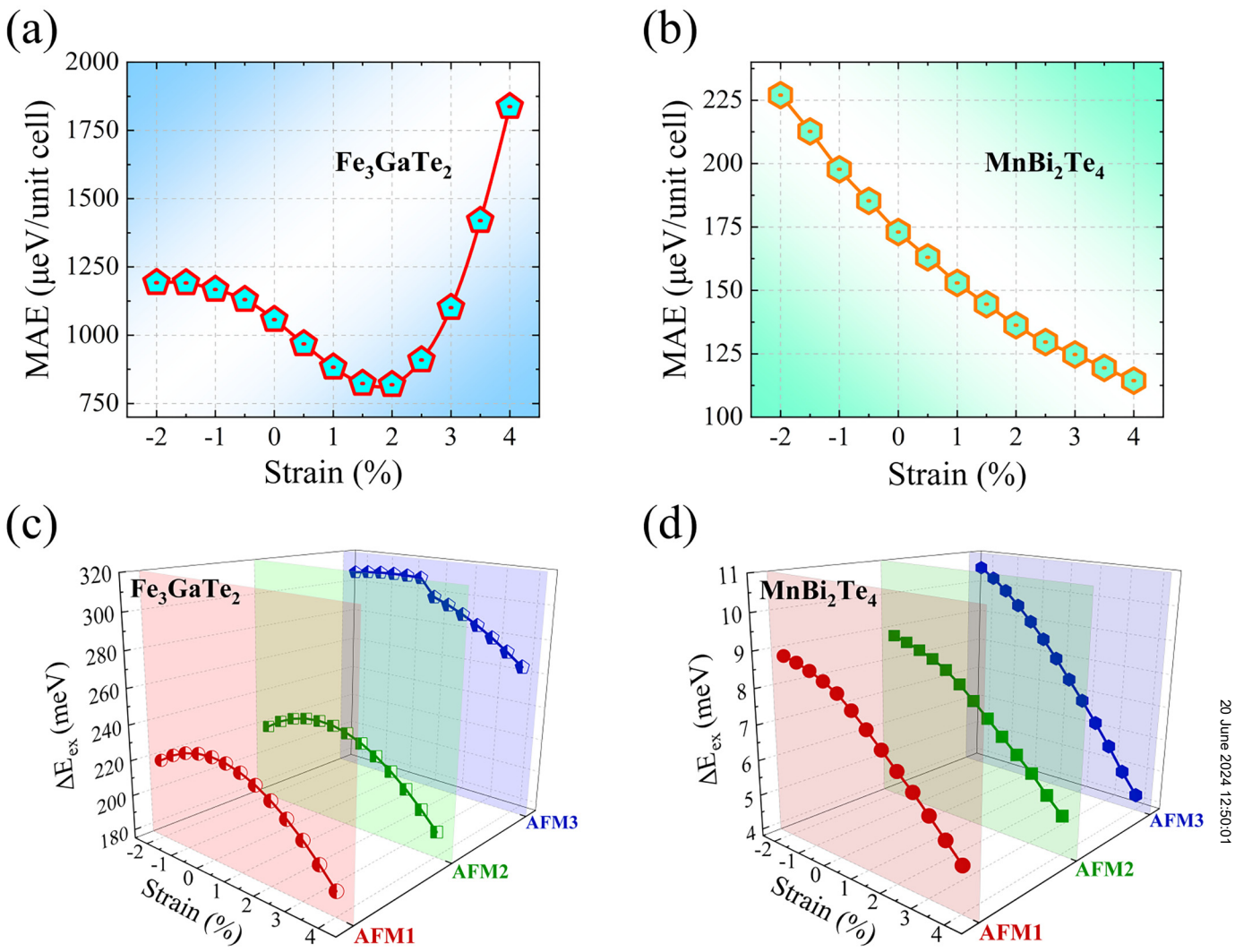

FIG. 2. Strain effect on the MAE and exchange energy (ΔE_{ex}) of monolayers. The MAE of the (a) Fe_3GaTe_2 and (b) $MnBi_2Te_4$ monolayers as a function of biaxial strain. Variations of ΔE_{ex} for the (c) Fe_3GaTe_2 and (d) $MnBi_2Te_4$ monolayers with biaxial strain.

resolved energy bands of the FM and AFM states for the device, respectively. It can be observed that Fe_3GaTe_2 and $MnBi_2Te_4$ within the device retain the energy band characteristics of metals and half-semiconductors compared with their freestanding layers [Figs. 1(b) and 1(e)], respectively. This indicates that the device exhibits a metallic property because of the presence of the metallic Fe_3GaTe_2, and each monolayer is connected through vdW interaction.

The influence of biaxial strain on the interlayer coupling of Fe_3GaTe_2/*h*-BN/$MnBi_2Te_4$ is explored. The coupling energy ΔE_{AFM-FM} is defined as $\Delta E_{AFM-FM} = E_{inter\_AFM} - E_{inter\_FM}$, where E_{inter_AFM} and E_{inter_FM} are the energies of Fe_3GaTe_2/*h*-BN/$MnBi_2Te_4$ in the AFM and FM states, respectively. As depicted in Fig. 3(c), the ΔE_{AFM-FM} increases monotonically with the applied strain, indicating that the magnetization state of the device tends to be FM for the tensile strain and AFM for the compressive strain. This suggests the possibility of controlling magnetization reversal by strain in the device. Importantly, there is almost no interlayer coupling between Fe_3GaTe_2 and $MnBi_2Te_4$ when the biaxial strain is zero. This essential phenomenon ensures that the magnetization reversal induced by strain is nonvolatile, meaning the magnetization state can be maintained in the device after removing the biaxial strain. Additionally, it is found that the magnitude of ΔE_{AFM-FM} can be tuned to around 0.2 and 0.1 meV with tensile and compressive strains, respectively. 0.1 meV corresponds to a magnetic field of 0.29 T due to the magnetic moment of Fe_3GaTe_2 being ~5.93 μ_B/f.u. Thus, the interlayer coupling induced by strain can overcome the coercivity ~0.1 T of Fe_3GaTe_2,[52] resulting in the reversal of the free Fe_3GaTe_2 layer. Therefore, the nonvolatile

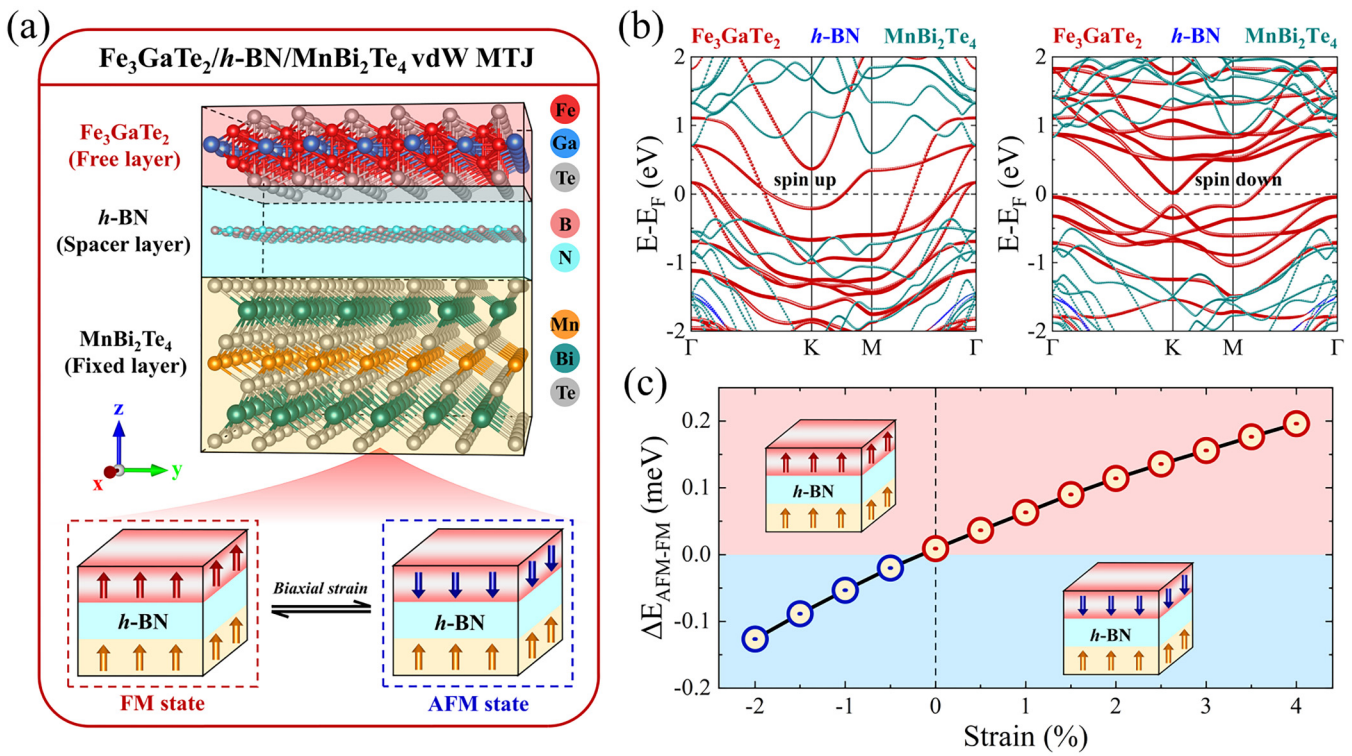

FIG. 3. Device structure, energy bands, and energy difference between AFM and FM states. (a) Schematic diagram of the structure and magnetization states for the Fe_3GaTe_2/*h*-BN/$MnBi_2Te_4$ device. (b) Spin- and atom-resolved energy bands of Fe_3GaTe_2/*h*-BN/$MnBi_2Te_4$ in the FM state. (c) Variation of energy difference between AFM and FM states for Fe_3GaTe_2/*h*-BN/$MnBi_2Te_4$ with biaxial strain.

magnetization reversal driven by strain can be realized in the Fe_3GaTe_2/*h*-BN/$MnBi_2Te_4$ device, which is highly expected for potentially writing the magnetization states in flexible spintronic devices. This novel approach shows promise for the development of advanced flexible spintronic devices with ultralow-power consumption and high-density storage capabilities.

The dependence of coupling strength (ΔE_{AFM-FM}) on biaxial strain in Fig. 3(c) can be understood by the superexchange theory.[57,58] In the literature, Zhu *et al.* theoretically demonstrated that the strain modulation of the bond angle and interlayer distance would affect the interlayer magnetic exchange, leading to the transition of interlayer coupling in bilayer MnS_2.[31] Sun *et al.* reported the interlayer magnetic transition from AFM to FM in few-layer VSe_2, which is attributed to the strain regulation of interlayer magnetic exchange.[59] For the present Fe_3GaTe_2/*h*-BN/$MnBi_2Te_4$ device, the interlayer magnetic coupling is mainly attributed to the exchange interactions between the *d* orbitals of Fe and Mn mediated by *p* and *s* orbitals. Figure 4(a) displays the crystal fields and splitting of *d* orbitals for Fe and Mn. Under the trigonal bipyramidal crystal field of D_{3h} symmetry, the five degenerated *d* orbitals of Fe should be split into a_1 (d_{z^2}), e_1 (d_{xz} and d_{yz}), and e_2 ($d_{x^2-y^2}$ and d_{xy}) states.[60] In the $MnBi_2Te_4$ monolayer, the *d* orbitals of Mn in an octahedral coordination environment are split into a doubly degenerate state e_g ($d_{x^2-y^2}$, d_{z^2}) and a triply degenerate state t_{2g} (d_{xy}, d_{xz}, d_{yz}).[61,62] In this case, there would exist two kinds of exchange paths involving four possible hopping channels, that is, e_g-*p*…*p*-a_1 and e_g-*p*…*p*-e_1 (path 1) and t_{2g}-*p*…*p*-a_1 and t_{2g}-*p*…*p*-e_1 (path 2), as illustrated in Fig. 4(b). Each channel is mediated by several *p* and one *s* orbitals across two vdW gaps. Notably, σ bonds are formed between e_g and *p* orbitals or a_1 and *p* orbitals, whose strengths are much stronger than that of π bonds formed between t_{2g} and *p* orbitals or e_1 and *p* orbitals.[63] Therefore, the e_g-*p*…*p*-a_1 channel of path 1 plays a dominant role in determining the interlayer magnetic coupling, as highlighted by the red frame in Fig. 4(b). The electron virtual hopping processes along the e_g-*p*…*p*-a_1 channel in Fig. S4 in the supplementary material shows the FM and AFM exchange interactions. When the biaxial strain is applied to the device, the strain would influence the competition between the FM and AFM interactions by changing the φ, as shown in the left of Fig. 4(b). The dependence of φ on biaxial strains is plotted in Fig. 4(c). The φ tends to 90° and 180° with the increase in the tensile and compressive strains, respectively. The insets draw the e_g-*p*…*p*-a_1 channel with φ of 90° and 180°, which correspond to the FM and AFM exchange coupling according to the Goodenough–Kanamori–Anderson (GKA) rule, respectively.[64–66] Thus, the interlayer coupling in the Fe_3GaTe_2/*h*-BN/$MnBi_2Te_4$ device favors the FM state under the tensile strain, while it favors the AFM state under the compressive strain. Without strain, AFM interaction is

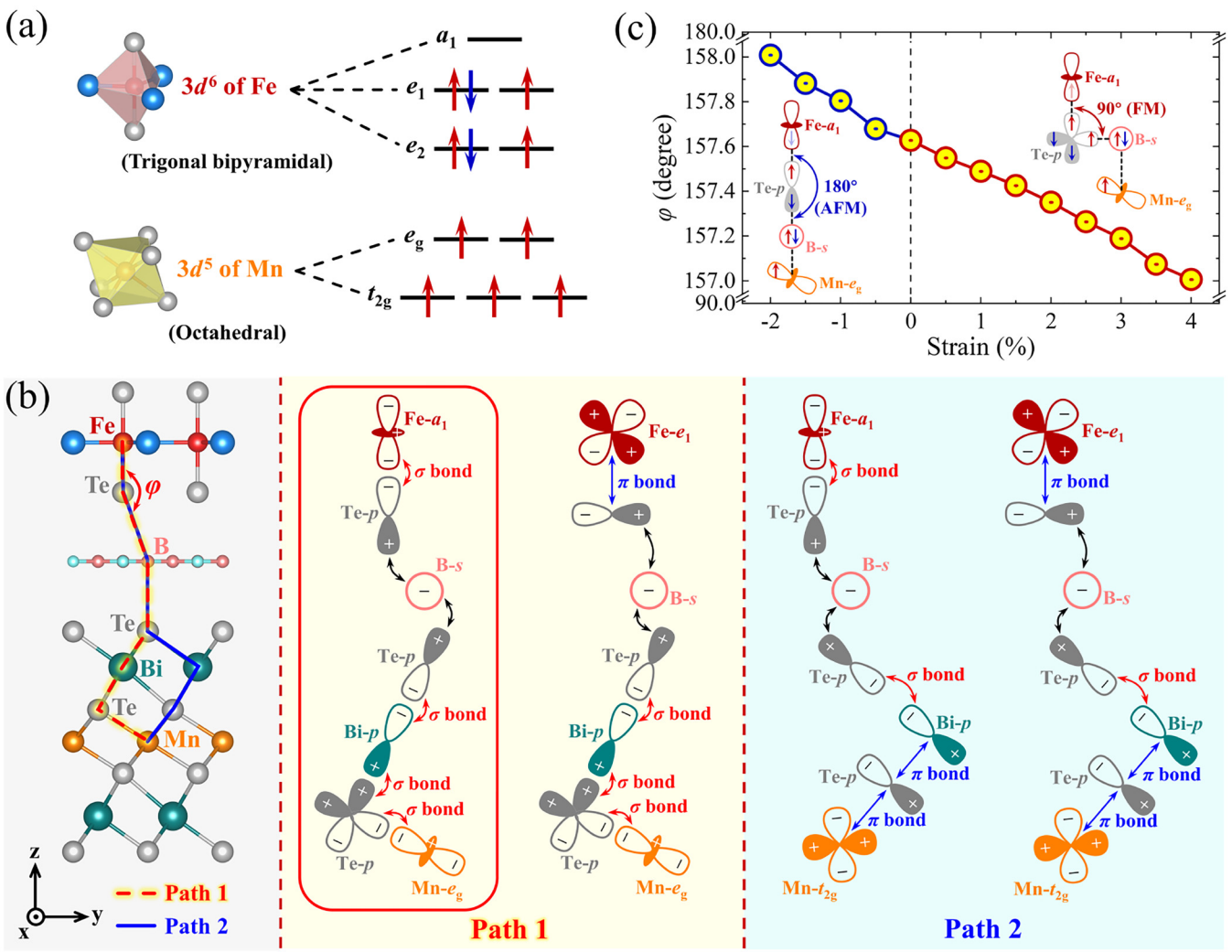

FIG. 4. Strain regulates interlayer magnetic exchange coupling. (a) Splitting of the *d* orbitals for Fe and Mn atoms under trigonal bipyramidal and octahedral crystal fields, respectively. (b) Interlayer exchange interactions between Fe_3GaTe_2 and $MnBi_2Te_4$ monolayers mediated by *p* and *s* orbitals across two vdW gaps. Only Fe atoms in the middle layer of Fe_3GaTe_2 are displayed here for simplicity. The φ is the angle of Fe–Te–B. (c) Dependence of φ on biaxial strains. The insets in the tensile and compressive strain regions refer to the cases where $\varphi = 90°$ and $\varphi = 180°$, respectively.

comparable to FM interaction, resulting in a near zero coupling by the competition between the AFM and FM interactions.

C. Reading magnetization states under strain

The storage of binary bits 0 and 1 in magnetic recording relies on the manipulation and detection of magnetization states in the magnetic recording media.[67,68] Writing of magnetization states regulated by strain has been achieved in the Fe_3GaTe_2/*h*-BN/$MnBi_2Te_4$ device. Now, it is crucial to detect the magnetization states in such a device for its practical application in information storage. The TMR effect is an effective means to read the magnetization states in spintronic devices.[15,69] To investigate the spin-dependent transport properties of the present device, a vdW MTJ of Gr/Fe_3GaTe_2/*h*-BN/$MnBi_2Te_4$/Gr is constructed, as shown in Fig. 5(a). The central scattering region includes four atomic layers of Gr on both sides. The arrows at the bottom show the magnetization directions of each magnetic layer for the FM and AFM states. In Fig. 5(b), the spin-resolved transmission spectra are shown for the device in the FM and AFM states without strain. The TMR effect of the device can be calculated using the following formula:[70]

$$\mathrm{TMR} = \frac{(T_{\mathrm{FM\_spin\text{-}up}} + T_{\mathrm{FM\_spin\text{-}down}}) - (T_{\mathrm{AFM\_spin\text{-}up}} + T_{\mathrm{AFM\_spin\text{-}down}})}{T_{\mathrm{FM\_spin\text{-}up}} + T_{\mathrm{FM\_spin\text{-}down}}} \times 100\%,$$

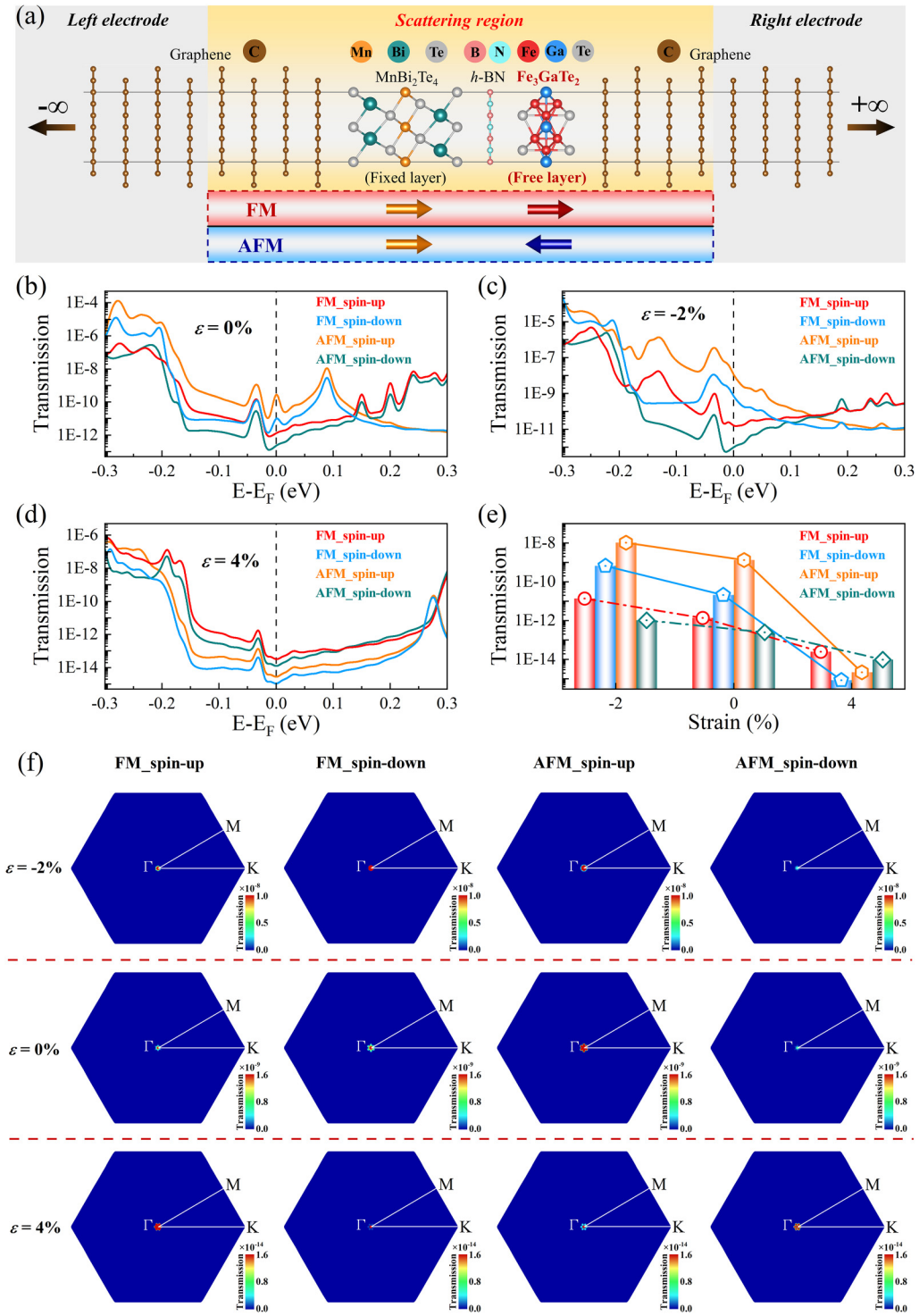

FIG. 5. Structure and transmission of the Gr/Fe_3GaTe_2/*h*-BN/$MnBi_2Te_4$/Gr device. (a) Schematic diagram of the model for the device. Spin-resolved transmission of the device with (b) 0%, (c) −2%, and (d) 4% biaxial strains. (e) Strain effect on the spin-resolved transmission of the device at the Fermi level. (f) $k_{||}$-resolved transmission of the device under different biaxial strains.

where $T_{FM\_spin\text{-}up}$ ($T_{AFM\_spin\text{-}up}$) and $T_{FM\_spin\text{-}down}$ ($T_{AFM\_spin\text{-}down}$) represent the transmission probability of spin-up and spin-down channels at the Fermi level when the device is in the FM (AFM) state, respectively. Based on the results of Fig. 5(b), the calculated TMR is up to −5745%, which has the potential to effectively read the magnetization states of the Fe_3GaTe_2 free layer. Thus, by combining this reading technique of the TMR effect with the previously demonstrated writing method of applying a strain, a flexible spintronic device with both high density and energy efficiency can be achieved.

The spin-dependent transport properties of the Gr/Fe_3GaTe_2/*h*-BN/$MnBi_2Te_4$/Gr device under different in-plane biaxial strains are further investigated. Figures 5(c) and 5(d) show the spin-resolved transmission spectra of the device under −2% and 4% strains, respectively. In Fig. 5(c), the TMR of the device with −2% strain remains negative and is calculated up to −1478%. Comparatively, the sign of TMR for 4% strain is reversed, and its value still exceeds 50% [Fig. 5(d)]. Although the magnitudes of TMR under both compressive and tensile strains decrease compared with the strain-free case, they are still sufficient for effectively reading the magnetization states of the present device in practical applications. To understand the reason for different strain effects on the TMR of the device, the spin-resolved transmission probabilities at the Fermi level for both the FM and AFM states under the −2%, 0%, and 4% strains are summarized in Fig. 5(e). Under the −2% compressive strain, the electron transmission probabilities of all transport channels increase slightly and remain similar to the case of the 0% strain. In contrast, the 4% tensile strain has a distinct influence on the transmission of four channels. The transmission probabilities of both the spin-up channel in the FM state and the spin-down channel in the AFM state (FM_spin-up and AFM_spin-down) decrease slightly, while there is a sharp decrease in the other two channels (FM_spin-down and AFM_spin-up). As a result, the electron transport in the device under the −2% (0%) and 4% strains is dominated by the AFM_spin-up and the FM_spin-up channels, respectively.

To further confirm the observed difference in electron transmission under different strains, the $k_{||}$-resolved transmissions of the four channels for the Gr/Fe_3GaTe_2/*h*-BN/$MnBi_2Te_4$/Gr device with the −2%, 0%, and 4% strains are plotted in Fig. 5(f). For the device under the −2% strain, the transmission probabilities of the four channels are similar to that of the 0% strain. Specifically, the spin-up channel for the AFM state exhibits the highest transmission probability, while the spin-down channel for the AFM state shows the lowest transmission probability. In the FM state, there is a slightly higher transmission in the spin-down channel compared with the spin-up channel. In contrast, the electron transmission in the device with the 4% strain shows a distinct difference from that of −2% and 0% strains. For the FM state, the spin-up channel has the highest transmission probability, while the spin-down channel has the lowest. Comparatively, for the AFM state, the transmission probability of the spin-down channel is slightly higher than that of the spin-up channel. These results agree with the observations at the Fermi level in Figs. 5(b)–5(d), validating the strain- and spin-dependent modulations of electron transport in the device. Furthermore, the transmission probabilities of the four channels under different strains in Fig. 5(f) are all concentrated around the Γ point, which is consistent with the $k_{||}$-resolved DOS of the Gr electrode in Fig. S5 in the supplementary material.

IV. CONCLUSIONS

The vdW MTJ of Fe_3GaTe_2/*h*-BN/$MnBi_2Te_4$ is designed based on the Fe_3GaTe_2 and $MnBi_2Te_4$ monolayers with a stable PMA and intralayer FM coupling under the strain. The nonvolatile magnetization reversal has been realized in the device by employing strain. The TMR effect is as large as −5745% without strain and remains significant even with −2% and 4% strains, allowing for effectively reading the magnetization states in the device. The current strategy offers an insight for designing flexible spintronic devices with both high-density storage and ultralow-power consumption.

SUPPLEMENTARY MATERIAL

See the supplementary material for the magnetic configurations of the Fe_3GaTe_2 and $MnBi_2Te_4$ monolayers, the relative energies of different stacking types for the two monolayer materials, the energy bands of the Fe_3GaTe_2/*h*-BN/$MnBi_2Te_4$ device in the AFM state, a schematic of virtual hopping along the e_g-p…p-a_1 channel between Fe and Mn atoms, and the $k_{||}$-resolved DOS of the Gr electrode under different biaxial strains.

ACKNOWLEDGMENTS

This work was supported by the National Natural Science Foundation of China (NNSFC) (Nos. 52271238 and 12261131506), the Liaoning Revitalization Talents Program (No. XLYC2002075), and the Research Funds for the Central Universities (No. N2402002).

AUTHOR DECLARATIONS

Conflict of nterest

The authors have no conflicts to disclose.

Author Contributions

Li Deng: Formal analysis (lead); Validation (lead); Writing – original draft (lead); Writing – review & editing (equal). **Xiang Yin:** Formal analysis (supporting); Validation (supporting). **Junwei Tong:** Formal analysis (supporting); Validation (supporting). **Yanzhao Wu:** Formal analysis (supporting); Validation (supporting). **Fubo Tian:** Formal analysis (supporting); Validation (supporting). **Xianmin Zhang:** Formal analysis (lead); Funding acquisition (lead); Supervision (lead); Validation (lead); Writing – original draft (lead); Writing – review & editing (lead).

DATA AVAILABILITY

The data that support the findings of this study are available from the corresponding author upon reasonable request.

REFERENCES

[1]T. Song, X. Cai, M. W.-Y. Tu, X. Zhang, B. Huang, N. P. Wilson, K. L. Seyler, L. Zhu, T. Taniguchi, K. Watanabe *et al.*, "Giant tunneling magnetoresistance in spin-filter van der Waals heterostructures," Science **360**, 1214–1218 (2018).
[2]D. R. Klein, D. MacNeill, J. L. Lado, D. Soriano, E. Navarro-Moratalla, K. Watanabe, T. Taniguchi, S. Manni, P. Canfield, J. Fernández-Rossier *et al.*,

"Probing magnetism in 2D van der Waals crystalline insulators via electron tunneling," Science **360**, 1218–1222 (2018).
[3]Z. Wang, D. Sapkota, T. Taniguchi, K. Watanabe, D. Mandrus, and A. F. Morpurgo, "Tunneling spin valves based on Fe_3GeTe_2/*h*-BN/Fe_3GeTe_2 van der Waals heterostructures," Nano Lett. **18**, 4303–4308 (2018).
[4]J.-F. Dayen, S. J. Ray, O. Karis, I. J. Vera-Marun, and M. V. Kamalakar, "Two-dimensional van der Waals spinterfaces and magnetic-interfaces," Appl. Phys. Rev. **7**, 011303 (2020).
[5]T. Miyazaki and N. Tezuka, "Giant magnetic tunneling effect in Fe/Al_2O_3/Fe junction," J. Magn. Magn. Mater. **139**, L231–L234 (1995).
[6]J. S. Moodera, L. R. Kinder, T. M. Wong, and R. Meservey, "Large magnetoresistance at room temperature in ferromagnetic thin film tunnel junctions," Phys. Rev. Lett. **74**, 3273–3276 (1995).
[7]S. S. P. Parkin, C. Kaiser, A. Panchula, P. M. Rice, B. Hughes, M. Samant, and S.-H. Yang, "Giant tunnelling magnetoresistance at room temperature with MgO (100) tunnel barriers," Nat. Mater. **3**, 862–867 (2004).
[8]S. Yuasa, T. Nagahama, A. Fukushima, Y. Suzuki, and K. Ando, "Giant room-temperature magnetoresistance in single-crystal Fe/MgO/Fe magnetic tunnel junctions," Nat. Mater. **3**, 868–871 (2004).
[9]S.-J. Liang, B. Cheng, X. Cui, and F. Miao, "Van der Waals heterostructures for high-performance device applications: Challenges and opportunities," Adv. Mater. **32**, 1903800 (2020).
[10]J. F. Sierra, J. Fabian, R. K. Kawakami, S. Roche, and S. O. Valenzuela, "Van der Waals heterostructures for spintronics and opto-spintronics," Nat. Nanotechnol. **16**, 856–868 (2021).
[11]L. M. Loong, W. Lee, X. Qiu, P. Yang, H. Kawai, M. Saeys, J.-H. Ahn, and H. Yang, "Flexible MgO barrier magnetic tunnel junctions," Adv. Mater. **28**, 4983–4990 (2016).
[12]W. Zhang, P. K. J. Wong, S. Jiang, Q. Chen, W. Huang, and A. T. S. Wee, "Integrating spin-based technologies with atomically controlled van der Waals interfaces," Mater. Today **51**, 350–364 (2021).
[13]C. Cardoso, D. Soriano, N. A. García-Martínez, and J. Fernández-Rossier, "Van der Waals spin valves," Phys. Rev. Lett. **121**, 067701 (2018).
[14]H. Li, S. Ruan, and Y.-J. Zeng, "Intrinsic van der Waals magnetic materials from bulk to the 2D limit: New frontiers of spintronics," Adv. Mater. **31**, 1900065 (2019).
[15]X. Li, J.-T. Lü, J. Zhang, L. You, Y. Su, and E. Y. Tsymbal, "Spin-dependent transport in van der Waals magnetic tunnel junctions with Fe_3GeTe_2 electrodes," Nano Lett. **19**, 5133–5139 (2019).
[16]Y. Su, X. Li, M. Zhu, J. Zhang, L. You, and E. Y. Tsymbal, "Van der Waals multiferroic tunnel junctions," Nano Lett. **21**, 175–181 (2021).
[17]H. Lin, F. Yan, C. Hu, Q. Lv, W. Zhu, Z. Wang, Z. Wei, K. Chang, and K. Wang, "Spin-valve effect in Fe_3GeTe_2/MoS_2/Fe_3GeTe_2 van der Waals heterostructures," ACS Appl. Mater. Interfaces **12**, 43921–43926 (2020).
[18]W. Zhu, H. Lin, F. Yan, C. Hu, Z. Wang, L. Zhao, Y. Deng, Z. R. Kudrynskyi, T. Zhou, Z. D. Kovalyuk *et al.*, "Large tunneling magnetoresistance in van der Waals ferromagnet/semiconductor heterojunctions," Adv. Mater. **33**, 2104658 (2021).
[19]W. Zhu, S. Xie, H. Lin, G. Zhang, H. Wu, T. Hu, Z. Wang, X. Zhang, J. Xu, Y. Wang *et al.*, "Large room-temperature magnetoresistance in van der Waals ferromagnet/semiconductor junctions," Chin. Phys. Lett. **39**, 128501 (2022).
[20]W. Zhu, Y. Zhu, T. Zhou, X. Zhang, H. Lin, Q. Cui, F. Yan, Z. Wang, Y. Deng, H. Yang *et al.*, "Large and tunable magnetoresistance in van der Waals ferromagnet/semiconductor junctions," Nat. Commun. **14**, 5371 (2023).
[21]W. Jin, G. Zhang, H. Wu, L. Yang, W. Zhang, and H. Chang, "Room-temperature spin-valve devices based on Fe_3GaTe_2/MoS_2/Fe_3GaTe_2 2D van der Waals heterojunctions," Nanoscale **15**, 5371–5378 (2023).
[22]H. Bai, X. Li, H. Pan, P. He, Z.-a. Xu, and Y. Lu, "Van der Waals antiferroelectric magnetic tunnel junction: A first-principles study of a $CrSe_2$/$CuInP_2S_6$/$CrSe_2$ junction," ACS Appl. Mater. Interfaces **13**, 60200–60208 (2021).
[23]J. Tong, Y. Wu, R. Zhang, L. Zhou, G. Qin, F. Tian, and X. Zhang, "Full-electrical writing and reading of magnetization states in a magnetic junction with symmetrical structure and antiparallel magnetic configuration," ACS Nano **15**, 12213–12221 (2021).
[24]S. Bandyopadhyay, J. Atulasimha, and A. Barman, "Magnetic straintronics: Manipulating the magnetization of magnetostrictive nanomagnets with strain for energy-efficient applications," Appl. Phys. Rev. **8**, 041323 (2021).
[25]L. Zhang, J. Zhou, H. Li, L. Shen, and Y. P. Feng, "Recent progress and challenges in magnetic tunnel junctions with 2D materials for spintronic applications," Appl. Phys. Rev. **8**, 021308 (2021).
[26]X. Lin, W. Yang, K. L. Wang, and W. Zhao, "Two-dimensional spintronics for low-power electronics," Nat. Electron. **2**, 274–283 (2019).
[27]F. Xue, C. Zhang, Y. Ma, Y. Wen, X. He, B. Yu, and X. Zhang, "Integrated memory devices based on 2D materials," Adv. Mater. **34**, 2201880 (2022).
[28]T. Song, Z. Fei, M. Yankowitz, Z. Lin, Q. Jiang, K. Hwangbo, Q. Zhang, B. Sun, T. Taniguchi, K. Watanabe *et al.*, "Switching 2D magnetic states via pressure tuning of layer stacking," Nat. Mater. **18**, 1298–1302 (2019).
[29]T. Li, S. Jiang, N. Sivadas, Z. Wang, Y. Xu, D. Weber, J. E. Goldberger, K. Watanabe, T. Taniguchi, C. J. Fennie *et al.*, "Pressure-controlled interlayer magnetism in atomically thin CrI_3," Nat. Mater. **18**, 1303–1308 (2019).
[30]J. Cenker, S. Sivakumar, K. Xie, A. Miller, P. Thijssen, Z. Liu, A. Dismukes, J. Fonseca, E. Anderson, X. Zhu *et al.*, "Reversible strain-induced magnetic phase transition in a van der Waals magnet," Nat. Nanotechnol. **17**, 256–261 (2022).
[31]W. Zhu, C. Song, Y. Zhou, Q. Wang, H. Bai, and F. Pan, "Insight into interlayer magnetic coupling in 1*T*-type transition metal dichalcogenides based on the stacking of nonmagnetic atoms," Phys. Rev. B **103**, 224404 (2021).
[32]H. Yang, S. O. Valenzuela, M. Chshiev, S. Couet, B. Dieny, B. Dlubak, A. Fert, K. Garello, M. Jamet, D.-E. Jeong *et al.*, "Two-dimensional materials prospects for non-volatile spintronic memories," Nature **606**, 663–673 (2022).
[33]H.-X. Cheng, J. Zhou, C. Wang, W. Ji, and Y.-N. Zhang, "Nonvolatile electric field control of magnetism in bilayer CrI_3 on monolayer In_2Se_3," Phys. Rev. B **104**, 064443 (2021).
[34]M. Fechner, P. Zahn, S. Ostanin, M. Bibes, and I. Mertig, "Switching magnetization by 180° with an electric field," Phys. Rev. Lett. **108**, 197206 (2012).
[35]S. Zhang, Y. G. Zhao, P. S. Li, J. J. Yang, S. Rizwan, J. X. Zhang, J. Seidel, T. L. Qu, Y. J. Yang, Z. L. Luo *et al.*, "Electric-field control of nonvolatile magnetization in $Co_{40}Fe_{40}B_{20}$/$Pb(Mg_{1/3}Nb_{2/3})_{0.7}Ti_{0.3}O_3$ structure at room temperature," Phys. Rev. Lett. **108**, 137203 (2012).
[36]J.-M. Hu, L.-Q. Chen, and C.-W. Nan, "Multiferroic heterostructures integrating ferroelectric and magnetic materials," Adv. Mater. **28**, 15–39 (2016).
[37]J. T. Heron, M. Trassin, K. Ashraf, M. Gajek, Q. He, S. Y. Yang, D. E. Nikonov, Y. H. Chu, S. Salahuddin, and R. Ramesh, "Electric-field-induced magnetization reversal in a ferromagnet-multiferroic heterostructure," Phys. Rev. Lett. **107**, 217202 (2011).
[38]D. Yu, Y. Ga, J. Liang, C. Jia, and H. Yang, "Voltage-controlled Dzyaloshinskii-Moriya interaction torque switching of perpendicular magnetization," Phys. Rev. Lett. **130**, 056701 (2023).
[39]G. Kresse and J. Furthmüller, "Efficient iterative schemes for *ab initio* total-energy calculations using a plane-wave basis set," Phys. Rev. B **54**, 11169–11186 (1996).
[40]G. Kresse and J. Furthmüller, "Efficiency of ab-initio total energy calculations for metals and semiconductors using a plane-wave basis set," Comput. Mater. Sci. **6**, 15–50 (1996).
[41]J. P. Perdew, K. Burke, and M. Ernzerhof, "Generalized gradient approximation made simple," Phys. Rev. Lett. **77**, 3865–3868 (1996).
[42]P. E. Blöchl, "Projector augmented-wave method," Phys. Rev. B **50**, 17953–17979 (1994).
[43]S. L. Dudarev, G. A. Botton, S. Y. Savrasov, C. J. Humphreys, and A. P. Sutton, "Electron-energy-loss spectra and the structural stability of nickel oxide: An LSDA+U study," Phys. Rev. B **57**, 1505–1509 (1998).
[44]H. J. Monkhorst and J. D. Pack, "Special points for Brillouin-zone integrations," Phys. Rev. B **13**, 5188–5192 (1976).
[45]S. Grimme, J. Antony, S. Ehrlich, and H. Krieg, "A consistent and accurate *ab initio* parametrization of density functional dispersion correction (DFT-D) for the 94 elements H-Pu," J. Chem. Phys. **132**, 154104 (2010).
[46]S. Grimme, S. Ehrlich, and L. Goerigk, "Effect of the damping function in dispersion corrected density functional theory," J. Comput. Chem. **32**, 1456–1465 (2011).

[47]V. Wang, N. Xu, J.-C. Liu, G. Tang, and W.-T. Geng, "VASPKIT: A user-friendly interface facilitating high-throughput computing and analysis using VASP code," Comput. Phys. Commun. **267**, 108033 (2021).
[48]M. Brandbyge, J.-L. Mozos, P. Ordejón, J. Taylor, and K. Stokbro, "Density-functional method for nonequilibrium electron transport," Phys. Rev. B **65**, 165401 (2002).
[49]M. S. José, A. Emilio, D. G. Julian, G. Alberto, J. Javier, O. Pablo, and S.-P. Daniel, "The SIESTA method for *ab initio* order-N materials simulation," J. Phys.: Condens. Matter **14**, 2745 (2002).
[50]N. Papior, N. Lorente, T. Frederiksen, A. García, and M. Brandbyge, "Improvements on non-equilibrium and transport Green function techniques: The next-generation transiesta," Comput. Phys. Commun. **212**, 8–24 (2017).
[51]N. Troullier and J. L. Martins, "Efficient pseudopotentials for plane-wave calculations," Phys. Rev. B **43**, 1993–2006 (1991).
[52]G. Zhang, F. Guo, H. Wu, X. Wen, L. Yang, W. Jin, W. Zhang, and H. Chang, "Above-room-temperature strong intrinsic ferromagnetism in 2D van der Waals Fe_3GaTe_2 with large perpendicular magnetic anisotropy," Nat. Commun. **13**, 5067 (2022).
[53]W. Jin, G. Zhang, H. Wu, L. Yang, W. Zhang, and H. Chang, "Room-temperature and tunable tunneling magnetoresistance in Fe_3GaTe_2-based 2D van der Waals heterojunctions," ACS Appl. Mater. Interfaces **15**, 36519–36526 (2023).
[54]M. M. Otrokov, I. I. Klimovskikh, H. Bentmann, D. Estyunin, A. Zeugner, Z. S. Aliev, S. Gaß, A. U. B. Wolter, A. V. Koroleva, A. M. Shikin *et al.*, "Prediction and observation of an antiferromagnetic topological insulator," Nature **576**, 416–422 (2019).
[55]Y. Deng, Y. Yu, M. Z. Shi, Z. Guo, Z. Xu, J. Wang, X. H. Chen, and Y. Zhang, "Quantum anomalous Hall effect in intrinsic magnetic topological insulator $MnBi_2Te_4$," Science **367**, 895–900 (2020).
[56]Y. An, K. Wang, S. Gong, Y. Hou, C. Ma, M. Zhu, C. Zhao, T. Wang, S. Ma, H. Wang *et al.*, "Nanodevices engineering and spin transport properties of $MnBi_2Te_4$ monolayer," npj Comput. Mater. **7**, 45 (2021).
[57]J. B. Goodenough, *Magnetism and the Chemical Bond* (Wiley-Interscience, New York, 1963).
[58]E. Pavarini, E. Koch, F. Anders, and M. Jarrell, *Correlated Electrons: From Models to Materials* (Forschungszentrums Jülich, Jülich, 2012).
[59]J. Sun, X. Jia, Y. Wang, and J. Zhang, "Strain-tunable magnetic transition in few-layer 1T-VSe_2," Appl. Phys. Lett. **121**, 072402 (2022).
[60]X. Jiang, Q. Liu, J. Xing, N. Liu, Y. Guo, Z. Liu, and J. Zhao, "Recent progress on 2D magnets: Fundamental mechanism, structural design and modification," Appl. Phys. Rev. **8**, 031305 (2021).
[61]H. Fu, C.-X. Liu, and B. Yan, "Exchange bias and quantum anomalous Hall effect in the $MnBi_2Te_4/CrI_3$ heterostructure," Sci. Adv. **6**, eaaz0948 (2020).
[62]G. Yu, C. Tang, Z. Tian, Z. Zhu, P. Liu, A. Pan, M. Chen, and X.-Q. Chen, "Ferroelectrically switchable magnetic multistates in $MnBi_2Te_4$ $(Bi_2Te_3)_n$ and $MnSb_2Te_4$ $(Sb_2Te_3)_n$ $(n = 0, 1)$ thin films," Phys. Rev. B **108**, 014106 (2023).
[63]Z. Li, J. Li, K. He, X. Wan, W. Duan, and Y. Xu, "Tunable interlayer magnetism and band topology in van der Waals heterostructures of $MnBi_2Te_4$-family materials," Phys. Rev. B **102**, 081107 (2020).
[64]J. B. Goodenough, "Theory of the role of covalence in the perovskite-type manganites [La, M(II)]MnO_3," Phys. Rev. **100**, 564–573 (1955).
[65]P. W. Anderson, "New approach to the theory of superexchange interactions," Phys. Rev. **115**, 2–13 (1959).
[66]J. Kanamori, "Crystal distortion in magnetic compounds," J. Appl. Phys. **31**, S14–S23 (1960).
[67]C. Chappert, A. Fert, and F. N. Van Dau, "The emergence of spin electronics in data storage," Nat. Mater. **6**, 813–823 (2007).
[68]A. Brataas, A. D. Kent, and H. Ohno, "Current-induced torques in magnetic materials," Nat. Mater. **11**, 372–381 (2012).
[69]K.-H. Min, D. H. Lee, S.-J. Choi, I.-H. Lee, J. Seo, D. W. Kim, K.-T. Ko, K. Watanabe, T. Taniguchi, D. H. Ha *et al.*, "Tunable spin injection and detection across a van der Waals interface," Nat. Mater. **21**, 1144–1149 (2022).
[70]J. M. De Teresa, A. Barthélémy, A. Fert, J. P. Contour, R. Lyonnet, F. Montaigne, P. Seneor, and A. Vaurès, "Inverse tunnel magnetoresistance in $Co/SrTiO_3/La_{0.7}Sr_{0.3}MnO_3$: New ideas on spin-polarized tunneling," Phys. Rev. Lett. **82**, 4288–4291 (1999).